Journal of Advanced Ceramics
2020, **9**(1): 107–122
https://doi.org/10.1007/s40145-019-0353-1
ISSN 2226-4108
CN 10-1154/TQ

Research Article

Photocatalytic degradation evaluation of N–Fe codoped aligned TiO_2 nanorods based on the effect of annealing temperature

Abbas Sadeghzadeh-Attar*

Department of Metallurgy and Materials Engineering, University of Kashan, P.O. Box. 87317-53153, Ghotb Ravandi Blvd., Kashan, Iran

Received: May 18, 2019; Revised: October 15, 2019; Accepted: October 18, 2019
© The Author(s) 2019.

Abstract: In this paper, a comparative study on the photocatalytic degradation of the Rhodamine B (RhB) dye as a model compound using N–Fe codoped TiO_2 nanorods under UV and visible-light ($\lambda \geqslant$ 420 nm) irradiations has been performed. TiO_2 photocatalysts were fabricated as aligned nanorod arrays by liquid-phase deposition process, annealed at different temperatures from 400 to 800 ℃. The effects of annealing temperature on the phase structure, crystallinity, BET surface area, and resulting photocatalytic activity of N–Fe codoped TiO_2 nanorods were also investigated. The degradation studies confirmed that the nanorods annealed at 600 ℃ composed of both anatase (79%) and rutile phases (21%) and offered the highest activity and stability among the series of nanorods, as it degraded 94.8% and 87.2% RhB in 120 min irradiation under UV and visible-light, respectively. Above 600 ℃, the photocatalytic performance of nanorods decreased owning to a phase change, decreased surface area and bandgap, and growth of TiO_2 crystallites induced by the annealing temperature. It is hoped that this work could provide precious information on the design of 1D catalyst materials with more superior photodegradation properties especially under visible-light for the further industrial applications.

Keywords: N–Fe codoped TiO_2 nanorods; liquid-phase deposition; annealing temperature; photocatalytic degradation

1 Introduction

As an n-type semiconductor, TiO_2 is an important material, which possesses good thermal and chemical stability, high oxidizing power, nontoxicity, and low cost [1]. Therefore, it is widely studied for its potential environmental applications, remarkable for the usage as photocatalyst to purify wastewater containing industry and toxic organic pollutants [2]. The major drawback of TiO_2 is its large band gap (3.0 eV for anatase phase and 3.2 eV for rutile phase), which allows it to absorb only a small portion of sunlight corresponding to the UV region of solar spectrum. On the other hand, the recombination rate of photo-generated electron and hole pairs in TiO_2 is high [3]. Hence, these conclude the low photocatalytic efficiency of TiO_2 in the visible region. To overcome the drawback of low photocatalytic efficiency, considerable efforts have been taken, such as dimensionality reduction [4], metal and non-metal doping [5], and semiconductor coupling [6]. One-dimensional (1D) TiO_2 nanostructures, including nanobelts, nanofibers, nanorods, nanowires, and nanotubes [7–11] can be considered as one of good

* Corresponding author.
E-mail: sadeghzadeh@kashanu.ac.ir

candidates for extending the activity of photocatalysts under sunlight [12,13]. They provide unique size-dependent properties, such as high electron mobility, directed electron transport, low carrier recombination rate, very high specific surface area, and excellent surface activity [14–18]. Although several template-based techniques such as electrophoretic deposition [19], sol–gel synthesis [20], chemical vapor deposition (CVD) [21], ALD [22], etc., have been employed to fabricate 1D TiO_2 nanostructures, liquid-phase deposition (LPD) process has been shown to be especially versatile synthesis procedure. This method is one of the simplest and most practical ones, since it has so many advantages such as mild reaction condition, high degree of control, simple equipment requirement, low cost, desired size and morphology, and allows TiO_2 films to be deposited over large areas [23,24]. TiO_2-rod shape has light scattering effect and can decouple the directions of light absorption and charge carrier collection. So, it enhances electron charge transport which is the critical issue in photoelectron chemical and photocatalysis applications [25,26]. On the other hand, coupling with other semiconductors [27], plasmonic coupling with noble metals [28], or doping with different metallic and non-metallic atoms have also been employed to improve photocatalytic efficiency. Typically, non-metallic elements such as C, N, S, P, and F can be used to substitute lattice oxygen anions [29–31], whereas metallic elements such as V, Cu, Zn, Bi, Co, and Fe substitute Ti cations [32–35]. These elements can create energy levels of the intermediate states in the band gap and act as electron trapper to inhibit the indirect recombination of photogenerated electrons and holes [36]. Furthermore, they can shift the optical absorption edge of TiO_2 to lower energy, and thereby extend the photoactive region to visible-light [37]. It is well known that the photocatalytic performance of TiO_2 depends strongly on the amount of doping and the annealing temperatures of samples [38]. Therefore, it seems necessary to study the effects of the annealing temperature on the phase structure, crystallinity, specific surface area, and resulting photocatalytic activity of N–Fe codoped TiO_2 nanorods. However, previous studies on the photocatalytic activity of TiO_2 nanostructures often use UV light as excited source for photodegradation of pollutants. Herein, N–Fe codoped TiO_2 nanorods with diameter about 100 nm were fabricated by LPD process. The as-prepared nanorods were then annealed at different temperatures. After that, the photocatalytic efficiency of the nanorods was evaluated by the photocatalytic degradation using Rhodamine B (RhB) as a model pollutant in the presence of UV and visible-light and quantification of the generated CO_2 as one of the main products.

2 Experimental

2.1 Preparation of N–Fe codoped TiO_2 nanorods

The materials that were used for fabricating the N–Fe codoped TiO_2 nanorods are ammonium hexafluorotitanate ($(NH_4)_2TiF_6$, 99.99%), iron nitrate ($Fe(NO_3)_3{\cdot}9H_2O$, ⩾ 98%), and ammonia solution (NH_4OH, 28%) purchased from Sigma-Aldrich Co. As a template and starting material, a commercial Whatman anodisc anodized alumina membrane (AAM) with straight nanoporous channels about 100 nm in diameter was used in the experimental. Ordered arrays of N–Fe codoped TiO_2 nanorods were prepared from treatment solutions by dissolving $(NH_4)_2TiF_6$ as a metal-fluoro complex in deionized water (18 μΩ) to a concentration of 0.1 $mol{\cdot}L^{-1}$. FeOOH–HF aqueous solution was used as the Fe source. This solution was prepared by adding NH_4OH to $Fe(NO_3)_3$ aqueous solution. Then, HF (48%, Sigma-Aldrich) was added to achieve the FeOOH–HF solution with a concentration of 0.05 $mol{\cdot}L^{-1}$. The treatment solution was prepared by mixing $(NH_4)_2TiF_6$ and FeOOH–HF in deionized water under stirring at room temperature for 30 min. In the following, AAM template was placed vertically into the aqueous treatment solution and temperature was maintained at room temperature for a certain deposition time. At the end of the deposition process, the samples containing the obtained nanorods were taken out from the solution, thoroughly washed carefully with ethanol and distilled water to remove residual solution. Free standing nanorod arrays were obtained by dissolving the AAM templates in a 4 $mol{\cdot}L^{-1}$ NaOH solution for 10 min, followed by washing and drying at 100 ℃ for 4 h. Formation of nanorods into the pores of the AAM templates is accompanied by the deposition of titanium hydroxide/oxyhydroxide on both sides of the AAM templates. To promote the dihydroxide/dioxyhydroxide reactions, enhance the interconnectivity of the particles, and yield the corresponding crystalline TiO_2 nanorods, the initially amorphous as-deposited N–Fe codoped TiO_2 nanorods by LPD process were annealed in air at 300, 400, 500, 600, 700, and 800 ℃ for 2 h. Pure TiO_2

nanorods were fabricated in a same procedure without use of N and Fe source annealed at 600 ℃ for 2 h.

2. 2 Characterization and photocatalytic property studies of N–Fe codoped TiO_2 nanorods

Thermal gravimetric analysis (TGA) and differential thermal analysis (DTA) of the as-deposited N–Fe codoped TiO_2 nanorods obtained by LPD process were recorded using a Netzsch STA 409 PC Luxx instrument. The measurements were performed at a heating rate of 10 ℃·min^{-1} from room temperature to 800 ℃ under a flowing air environment. The analysis of the morphologies of alumina membranes and N–Fe codoped TiO_2 nanorod arrays was obtained by field emission scanning electron microscope (FESEM, TESCAN MIRA3, operating at 15 kV). The microscopic features of the samples were performed by transmission electron microscopy (TEM) and high-resolution transmission electron microscopy (HRTEM). The observations were carried out with a Hitachi 80 instrument working at 200 kV accelerating voltage. The specimens for TEM were prepared by dispersing the final products in ethanol, and then a drop of the suspension was placed on a carbon copper grid. The X-ray diffraction (XRD) patterns of the resulting nanorods were collected with an X'pert Philips MPD diffractometer, equipped with a Cu Kα radiation (λ = 1.5402 Å) from 20° to 90°. X-ray photoelectron spectroscopy (XPS) analysis was measured by a PHI-5700 ESCA system with a monochromatic Al Kα radiation source ($h\upsilon$ = 1486.6 eV). The X-ray source was run at a 30 mA emission current and 10 kV anode bias, while the electron energy analyzer operated at the constant pass energy of 50 eV. The binding energies were normalized with respect to adventitious C (1s) due to amorphous carbon, which was assigned to a binding energy of 284.6 eV. The specific surface area and pore size of the samples were evaluated by the nitrogen gas adsorption analyzer model BELSORP mini II at 77 K. The 0.1 g samples were degassed at 120 ℃ for 10 h to remove surface moisture before measurements.

The photocatalytic activities of the N–Fe codoped TiO_2 nanorods were evaluated in the photocatalytic degradation of RhB dye. The experimentals were carried out in the dark, visible-light, and UV light irradiations without any catalyst (blank), and in the presence of TiO_2 nanorod photocatalysts. A 300 W xenon lamp was employed as the UV light source, while for visible irradiation, wavelengths higher or equal to 420 nm were allowed to enter the reactor by using a proper cut-off filter. The initial concentration of RhB dye was 20 mg·L^{-1} and the dosage of TiO_2 photocatalyst was 100 mg per 200 mL of dye solution. Before exposure to illumination in the glass beaker, the suspension solution was magnetically stirred in darkness for 90 min to ensure adsorption/desorption equilibrium of the dye on the nanorod surfaces. During the reaction, the solution was maintained at room temperature and distance between lamp and the top of the solution was 20 cm. At 30 min time interval of irradiation, 5 mL of the suspension was withdrawn over irradiation time of 120 min. The variations in the absorbance of RhB dye solution were monitored by using a LAMBDA25 UV–vis spectrophotometer. For comparison, commercial P25 nanoparticles from Degussa which is well-known high-performance photocatalyst, were also used to evaluate the photocatalytic activity. The P25 nanoparticles had particle size of 20 nm and specific surface area of about 50 m^2/g. The generated CO_2 of the photocatalytic reactions was analyzed by a Varian BV CP 3800 gas chromatography at room temperature. The 400 cm^3 gaseous products in the reaction cell were removed by a gas syringe at 30 min periodic intervals.

3 Results and discussions

3. 1 Structural and morphological characteristics of N–Fe codoped TiO_2 nanorods

The fulfillment of the template-directed LPD process for the synthesis of N–Fe codoped TiO_2 nanorod arrays was schematically presented in Fig. 1(a). When the alumina template is immersed in the treated solution, the internal surface of template pores directly contact with the treatment solution and then alumina template dissolves. Hydrous-TiO_2 deposits in situ on the templates that is accompanied with the consumption of alumina templates. Thus the internal surface of nanosized pores is covered with TiO_2 nanoparticles, which leads to formation of nanotubes [39]. As the reaction continues, the pores are completely filled and the N–Fe codoped TiO_2 nanorod arrays are formed. The inset upper right FESEM image in Fig. 1(a) illustrates a typical surface morphology of the commercial alumina template. It is composed of many nanopores, and the average size of the pores is about 80–100 nm.

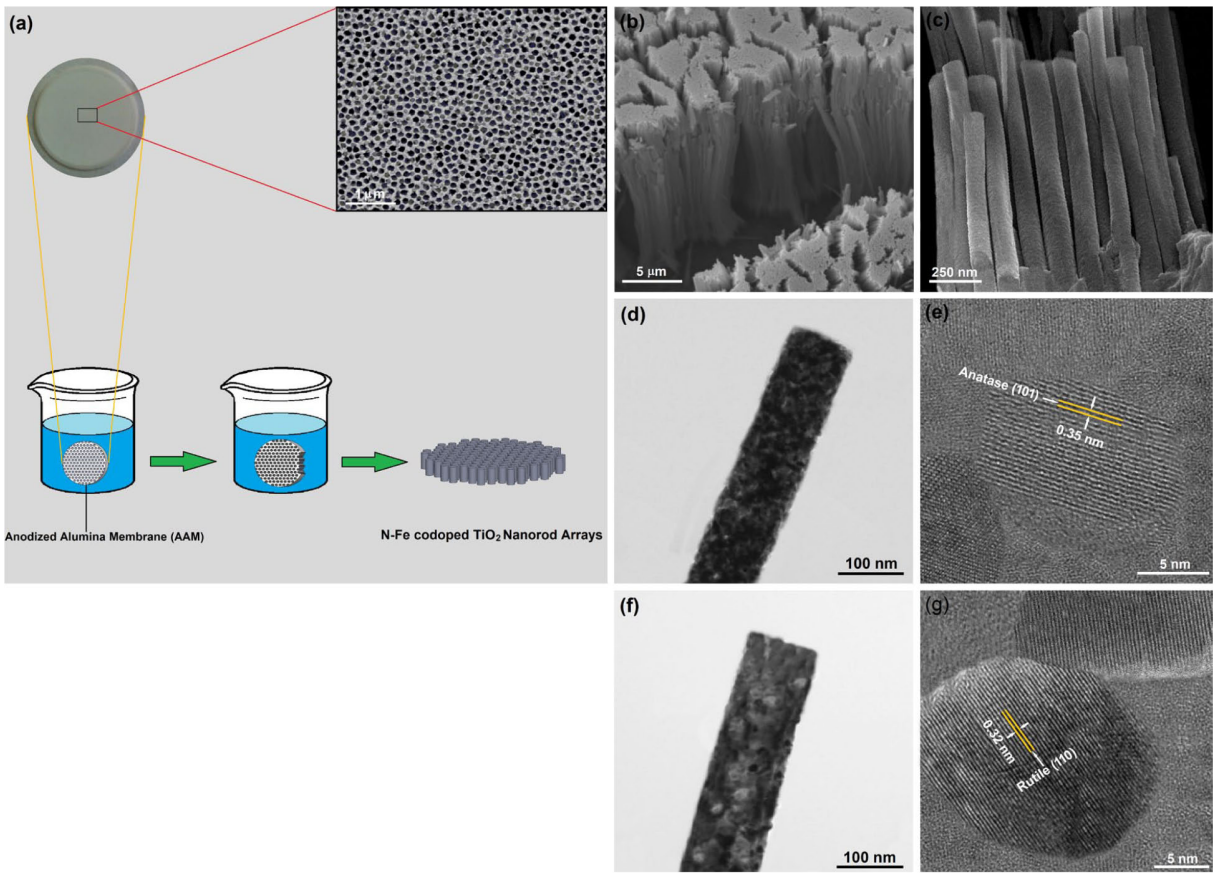

Fig. 1 (a) Schematic illustration for the formation of N–Fe codoped TiO_2 nanorod arrays via template-directed LPD (inset presents surface-view FESEM image of AAM template). (b, c) Typical low and high magnification FESEM images of the N–Fe codoped TiO_2 nanorod arrays. (d, e) TEM and HRTEM images of the individual N–Fe codoped nanorod annealed at 600 ℃ for 2 h. (f, g) TEM and HRTEM images of the individual N–Fe codoped nanorod annealed at 800 ℃ for 2 h.

Figures 1(b) and 1(c) display the FESEM images of N–Fe codoped TiO_2 nanorod arrays prepared by LPD process in the alumina template under different magnifications. It can be observed that the nanorods are smooth and close to each other. The average diameter of resultant nanorods is about 80–100 nm whereas the length of them is about 12 μm, which are comparable to the dimensions of the alumina template pores. This is a main reason that the alumina templates serve as a suitable starting material for the fabrication of aligned 1D TiO_2 nanostructures. Figure 1(d) shows the TEM image of the single N–Fe codoped TiO_2 nanorod annealed at 600 ℃ for 2 h after the removal of the alumina template in a 6 mol·L^{-1} NaOH solution. The polycrystalline TiO_2 nanorod has uniform diameters (~100 nm) and the rod surface is made up of many small nanoparticles about 10 nm in size. The HRTEM image taken from the nanorod is presented in Fig. 1(e) and further reveals its detailed crystallographic structure. The interplanar spacing is 0.35 nm which corresponds to the *d*-spacing of (101) lattice plane of the tetragonal anataseTiO_2 crystal.

The TEM image in Fig. 1(f) also shows a single N–Fe codoped TiO_2 nanorod annealed at 800 ℃ for 2 h. The surface of rod is smooth with a diameter about 100 nm equal to the pore size of alumina template. The HRTEM image of nanorod revealed in Fig. 1(g) confirms that it is polycrystalline, with lattice *d*-spacing of 0.32 nm, coinciding with the (110) plane spacing in the rutile TiO_2 structure.

The thermal behavior of samples collected by scratching the N–Fe codoped TiO_2 nanorods is given in Fig. 2. The TGA curve exhibits a very well-defined decrease in the mass of nanorods divided into three stages. The first weight loss of approximately 13.9% is appeared from room temperature to 230 ℃, which can be corresponded to the elimination of the hydrated water molecules and other chemicals. The second main weight loss of about 22.7% occurs between 260 and 392 ℃, which is associated with the thermal decomposition

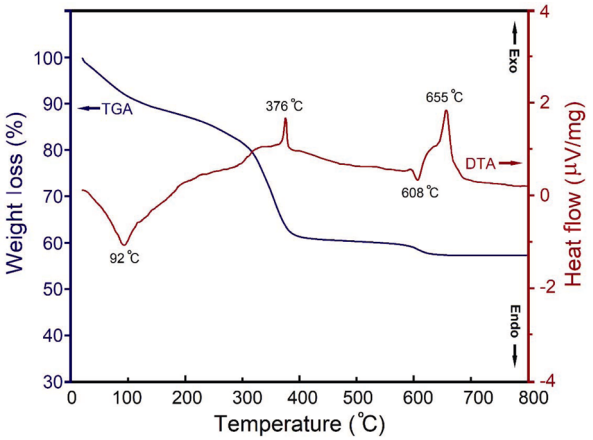

Fig. 2 TGA and DTA curves of the as-deposited N–Fe codoped TiO_2 nanorods obtained by LPD process with a heating rate of 10 ℃·min^{-1} in an air flow.

of the intermediate complex containing NH^{4+} and F^- in the nanorods [40]. The final stage from 590 to 625 ℃ with the mass loss of about 2.1% may be due to the dehydration of chemisorbed water in the Ti complex. Over 625 ℃ the weight loss curve levels off. These thermal events are also observed in the DTA curve which reveals two endothermic peaks at 92 and 608 ℃. These peaks are indicative of the transition from the metal hydroxide products to the crystalline N–Fe codoped TiO_2 nanorods. The sharp exothermic reaction peaks observed at ca. 376 and 655 ℃ in DTA curve are presumably due to the latent heat for the phase change of the N–Fe codoped TiO_2 nanorods from amorphous to crystalline anatase phase and anatase to rutile phase, respectively.

The nanorods obtained by hydrolysis reaction of TiF_6^{-2} ions at room temperature have poor photodegradation properties due to the weak crystallization. Thus, the N–Fe codoped TiO_2 nanorods fabricated by the LPD process must be annealed at high temperatures in order to enhance crystallization and eliminate impurities. The influence of annealing temperature on the crystallization behavior of nanorod arrays, crystal phase identification, and the estimation of the anatase–rutile ratio and the crystallite size of each phase present were determined by XRD. Figure 3 reveals diffraction patterns of the P25 Degussa, undoped TiO_2 nanorods, and N–Fe codoped TiO_2 nanorods after thermal treatment at different temperatures from 300 to 800 ℃. XRD pattern of the P25 confirmed the presence of anatase mixed with rutile phase, in agreement with the standard diffraction data as certified by Sigma-

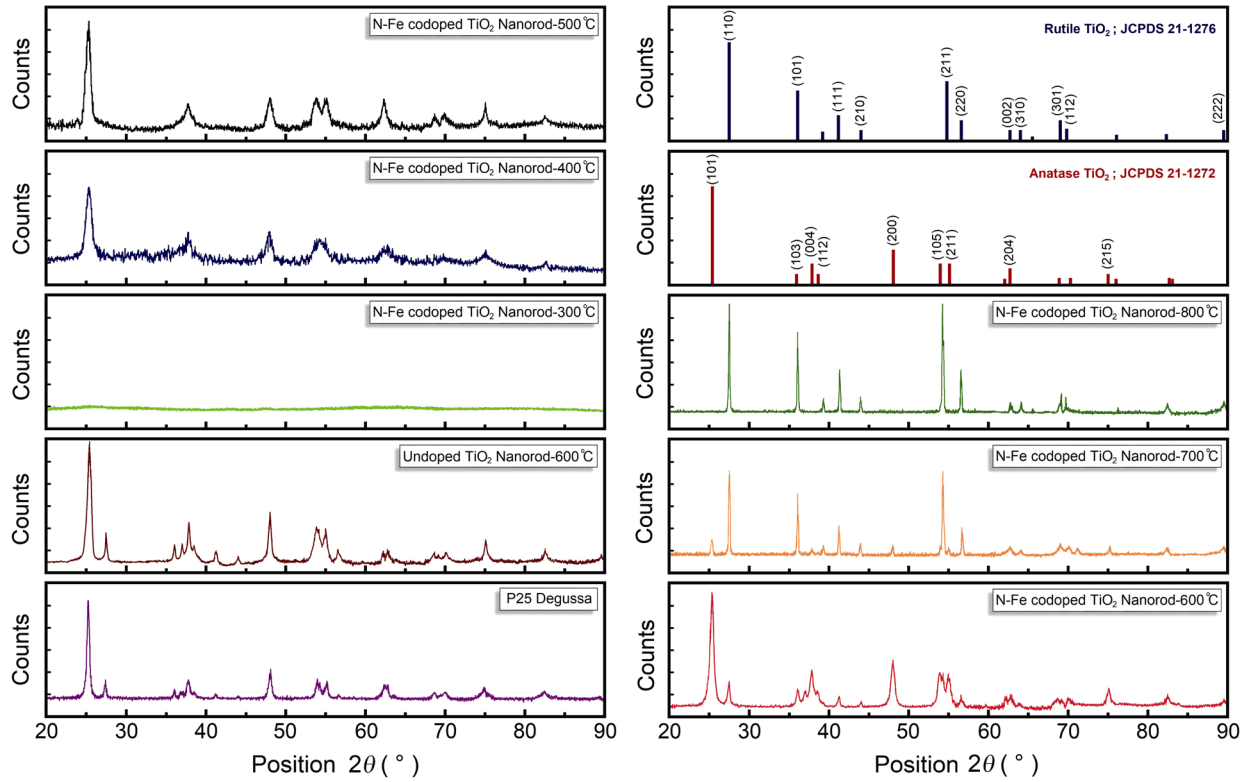

Fig. 3 Typical XRD patterns of P25 nanoparticles, undoped TiO_2 nanorod, and N–Fe codoped TiO_2 nanorods annealed at different temperatures from 300 to 800 ℃.

Aldrich producer. The XRD pattern of N–Fe codoped TiO_2 nanorods annealed at 300 ℃ indicated that this nanorods were amorphous since no TiO_2 crystalline peaks were recorded in the pattern. From the XRD pattern of the nanorods annealed at 400 ℃, only peaks that correspond to the polycrystalline anatase-type TiO_2 could be observed (JCPDS Card No. 21-1272). No peaks related to metallic iron, iron oxides, or/and any impurity phases were detected, demonstrating the nanorods are well crystallized. The broad width of XRD peaks indicates formation of nanosized particles. With increasing annealing temperature up to 500 ℃, the intensity of peaks increases and the width of the peaks becomes narrow, indicating improvement of crystallization and the growth of crystallites. The particles grow rapidly with annealing treatment since they gain higher energy than the growth activation energy.

The XRD pattern of the nanorods annealed at 600 ℃ reveals the anatase phase and emerging peaks of rutile phase, indicating that the sample contains a mixture of anatase and rutile. This shows the occurrence of phase transformation from anatase to rutile. Annealing at 700 ℃ resulted in the change of the peak intensities for both phases. The intensity of the rutile peak increased, while that of anatase peak gradually became weak, when annealing temperature increased. The phase composition of mixed phase N–Fe codoped TiO_2 nanorods can be determined from XRD patterns according to formula [41]:

$$W_R = (1 + 0.8I_A/I_R)^{-1} \quad (1)$$

where W_R is the weight fraction of rutile in the nanorods, and I_A and I_R are the integrated intensity of anatase (101) peak and of rutile (110) peak, respectively. The amount of rutile phase in N–Fe codoped TiO_2 nanorods annealed at 600 ℃ was calculated 21 wt%, while in TiO_2 nanorods annealed at 600 ℃ was 23.2 wt%. The lower amount of rutile phase in N–Fe codoped TiO_2 nanorods than that of the undoped TiO_2 nanorods can be attributed to the formation of Ti–O–Fe bonds. The Fe–O species at the interface of TiO_2 crystallites prevented the formation of rutile phase by inhibiting the nucleation. At 700 ℃, the amount of rutile phase in N–Fe codoped TiO_2 nanorods was estimated 86.4 wt%. Dam *et al.* [42] reported TiO_2 nanopowders consist of 83.63% anatase and 16.37% rutile at the annealing temperature of 650 ℃. Boehme and Ensinger [43] prepared the TiO_2 nanotubes at an annealing temperature of 583 K, consisting of 75% anatase and 25% rutile determined from data recorded on a standard powder diffractometer. For the sample annealed at 800 ℃, it can be clearly observed that the peaks associated with anatase phase are disappeared and only the rutile diffraction peaks as a major phase are dominated (JCPDS Card No. 21-1276). The rutile illustrates sharp XRD peaks without signs of broadening. In addition no characteristic peak of iron oxide phases was found for all N–Fe codoped TiO_2 nanorods, that can be ascribed to the incorporation of Fe atoms into the crystal lattice of TiO_2 during deposition. No significant difference in the position of the main anatase peak was also found, which it was attributed to the small difference in the size of Fe^{3+} (0.64 Å) and Ti^{4+} (0.68 Å) ions [35]. About the doped N atoms, their concentration might be too low to cause a shift in peak positions, although N has a larger ionic radius (1.71 Å) than replaced oxygen atom (1.32 Å) [44].

The crystallinity of the anatase and rutile structures distinctly improved with increasing annealing temperature, as seen from decrease in the full width-at-half-maximum (FWHM) of the diffraction peaks. Based on the Debye–Scherrer relation from the main diffraction peaks ((101) reflection for anatase and (110) reflection for rutile), the crystallite size of anatase increased from 8.1 to 32.3 nm, as the annealing temperature increased from 400 to 700 ℃. Meanwhile, for rutile it changed from 16.3 to 54.2 nm with increasing the annealing temperature from 600 to 800 ℃.

The XPS technique was applied to verify changes in chemical composition that happened due to the substitution of Ti for N and Fe atoms. The overall core level XPS survey spectra of undoped TiO_2 nanorod and N–Fe codoped TiO_2 nanorods annealed at different temperature ranging from 400 to 800 ℃ are shown in Fig. 4(a). The XPS spectrum for TiO_2 nanorod reveals that the sample contains Ti and O elements along with adventitious carbon. The N–Fe codoped TiO_2 nanorods contained not only Ti, O, and C elements, but also N and Fe. The present of nitrogen in the nanorods was corroborated by a single peak (N 1s spectrum) around 400 eV, which can be related to the formation of N^- anions incorporated in the TiO_2 as O–Ti–N structure feature [45]. Figure 4(b) illustrates the high resolution XPS spectra of the Fe 2p region taken on surface of the N–Fe codoped TiO_2 nanorods annealed at 400–800 ℃. It was found from the binding energies of nanorod annealed at 400 ℃ that the peaks located at 723.3 and 711.5 eV are assigned to the Fe $2p_{1/2}$ and Fe $2p_{3/2}$, respectively., indicating the chemical valent state of Fe is +3 (Fe^{3+}) [46]. It is well known that ionic radii of

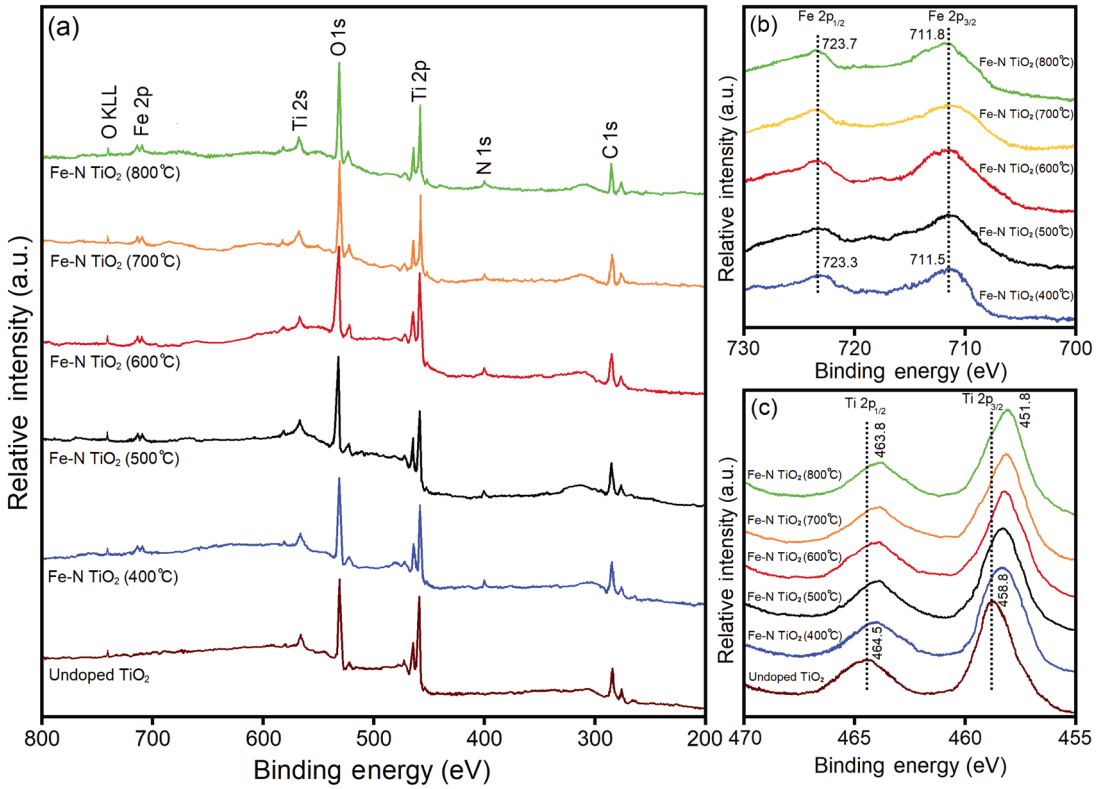

Fig. 4 (a) Overall core level XPS survey spectra, (b) high-resolution XPS spectra of the Fe 2p region, and (c) high-resolution XPS spectra of the Ti 2p region of of undoped TiO_2 nanorod annealed at 600 ℃ and N–Fe codoped TiO_2 nanorods annealed at 400, 500, 600, 700, and 800 ℃.

Ti^{4+} and Fe^{3+} are similar and that Fe^{3+} ions can be replaced to the lattice of TiO_2, resulting in the formation of Ti–O–Fe bonds in Fe–N codoped TiO_2 nanorods. The binding energies of the Fe 2p peaks show a positive shift with the increase of annealing temperature. The values of binding energy of Fe $2p_{3/2}$ exhibited a significant different from those of metallic Fe (707 eV), FeO (709.5 eV), and Fe_3O_4 (710.4 eV), indicating that iron and/or iron oxide species is not formed [47]. Furthermore, Fig. 4(c) presents the high resolution XPS of the Ti 2p region for TiO_2 nanorod and N–Fe codoped TiO_2 nanorods, respectively. The Ti 2p spectra in undoped TiO_2 nanorod show that Ti $2p_{3/2}$ and Ti $2p_{1/2}$ peaks at 458.8 and 464.5 eV, respectively, attributed Ti^{4+} [46]. The peak positions of both the Ti 2p core level in N–Fe codoped TiO_2 nanorods were shifted to a lower binding energy compared to undoped TiO_2 nanorod. This suggests that some Ti^{4+} ions are changed to a lower oxidation state, and thereby TiO_2 lattice is modified due to N and Fe substitution. Lower binding energy can also be explained on the basis of the formation of Fe–O–Ti and N–O–Ti bonds in the framework of TiO_2 [45]. The weight percentages of detected Fe and N dopants within the undoped TiO_2 nanorod and N–Fe codoped TiO_2 nanorods after annealing at various temperatures are listed in Table 1.

3.2 Surface area and pore size distributions of N–Fe codoped TiO_2 nanorods

Photcatalytic efficiency depends on several factors such as the total surface area, crystallinity, morphology, particle/pore size, type of porosity, and high reactivity of facets [48,49]. To further understand the difference between the photocatalytic behavior of N–Fe codoped TiO_2 nanorods annealed at different temperatures, we first focus on the effect of surface area. Figure 5 shows the specific surface area of the N–Fe codoped TiO_2 nanorods estimated according to standard multi-point Brunauer–Emmett–Teller (BET) method using nitrogen adsorption/desorption isotherms. All of the samples illustrate a similar type adsorption/desorption isotherm behavior with a type of hysteresis loop. According to the IUPAC classifications [50], the gas adsorption/desorption isotherms are normally divided into six categories and hysteresis loops into four types. In our work, the isotherm curves with the distinct hysteresis loops can be

Table 1 Textural properties of N–Fe codoped TiO_2 nanorods fabricated via template-directed LPD process annealed at different temperatures

Sample[a]	Specific surface area[b] (m^2/g)	D_{BET}[c] (nm)	Average pore size[d] (nm)	Crystallite size[e] (nm)		Doping concentration[f]	
				Anatase (101)	Rutile (110)	Fe (wt%)	N (wt%)
Undoped TiO_2-600 ℃	94.2	17.9	22	14.7	18.6	—	—
N–Fe–TiO_2-400 ℃	136.5	11.6	10	8.1	—	5.74	4.13
N–Fe–TiO_2-500 ℃	124.6	13.8	12	10.1	—	5.75	4.55
N–Fe–TiO_2-600 ℃	98.1	15.7	20	13.4	16.3	5.72	4.38
N–Fe–TiO_2-700 ℃	48.2	30.4	47	32.3	40.5	5.71	4.07
N–Fe–TiO_2-800 ℃	43.0	33.2	50	—	54.2	5.70	4.10

[a] The sample name represents of the N–Fe codoped TiO_2 nanorods annealed at different temperatures.
[b] Specific surface area estimated by the BET method.
[c] Average crystallite size estimated by the BET method.
[d] Average pore size estimated by the BJH method.
[e] Average crystallite size estimated by Scherrer's equation from XRD analysis.

characteristic of type IV, which suggests the presence of mesoporous materials with uniform size and shape of pores. Such type of mesoporous structure with a high specific surface area can be beneficial for applications as the photocatalysts.

The adsorption–desorption isotherms reveal that N_2 adsorption volume gradually increased as relative pressure P/P_0 increased. At relative pressure more than 0.9, the sharp increase in the adsorption volume is due to the present of mesoporous TiO_2 formed in the wall of nanorods. With increasing annealing temperature, the hysteresis loop shifted to higher relative pressure region. The specific BET surface area of undoped TiO_2 nanorod, and N–Fe codoped TiO_2 nanorods annealed at 400, 500, 600, 700, and 800 ℃ are estimated 94.2, 136.5, 124.6, 98.1, 48.2, and 43 m^2/g, respectively. The results show adsorbed volume reduced against the increase of the annealing temperatures, which leads to the decreasing in specific surface area. Since the specific surface area of the 1D TiO_2 nanostructures should depend on the size of aggregated TiO_2 nanoparticles, as the particle size became larger, the specific BET surface area would decrease. Assuming that the particles have spherical shape with the uniform size, specific surface areas of the powder can be related to the crystallite size according to following equation [51]:

$$D = 6000/(\rho S) \quad (2)$$

where D is average crystallite size (nm) estimated by BET, ρ is the theoretical density of TiO_2 (~3.8 g/cm^3 for anatase and ~4.2 g/cm^3 for rutile), and S is the specific surface area at corresponding temperature (m^2/g). As shown in Table 1, the estimated crystallite size of N–Fe codoped TiO_2 nanorods increased with increasing annealing temperature. The decrease in crystallite size leads to an increase of surface area and consequently a decrease of electron–hole recombination, producing more efficient separation of photogenerated electron–hole pairs.

The insets in Fig. 5 indicate the corresponding pore size distribution curves, which were derived by calculations based on the Barrett–Joyner–Halenda (BJH) method. It can be seen the pore size distribution peak became progressively broader with increasing the annealing temperature. The undoped TiO_2 nanorod indicated average pore size of about 22 nm (inset in Fig. 5(a)). The average pore size of the mesoporous N–Fe codoped TiO_2 nanorods remarkably increases from 10 to 50 nm, as the annealing temperature elevates from 400 to 800 ℃ (insets in Figs. 5(b)–5(f)). The specific BET surface area, average pore size, and crystallite size calculate by BET and XRD for N–Fe codoped TiO_2 nanorods annealed at different temperatures are listed in Table 1.

3.3 Photocatalytic activity of N–Fe codoped TiO_2 nanorods

The evolution of photocatalytic activity of the N–Fe codoped TiO_2 nanorod samples was tested by photo-assisted degradation of dye aqueous solutions under UV and visible-light irradiations. RhB was chosen as a representative dye to evaluate the photocatalytic degradation performance of the samples. Such toxic and mutagenic compounds in textile industry wastewaters are serious environmental problems due to their high chemical oxygen demand content, unacceptable color, and resistance to chemical degradation. All experiments were carried out at the natural pH of the dyes at room temperature, and similar experiments were also performed

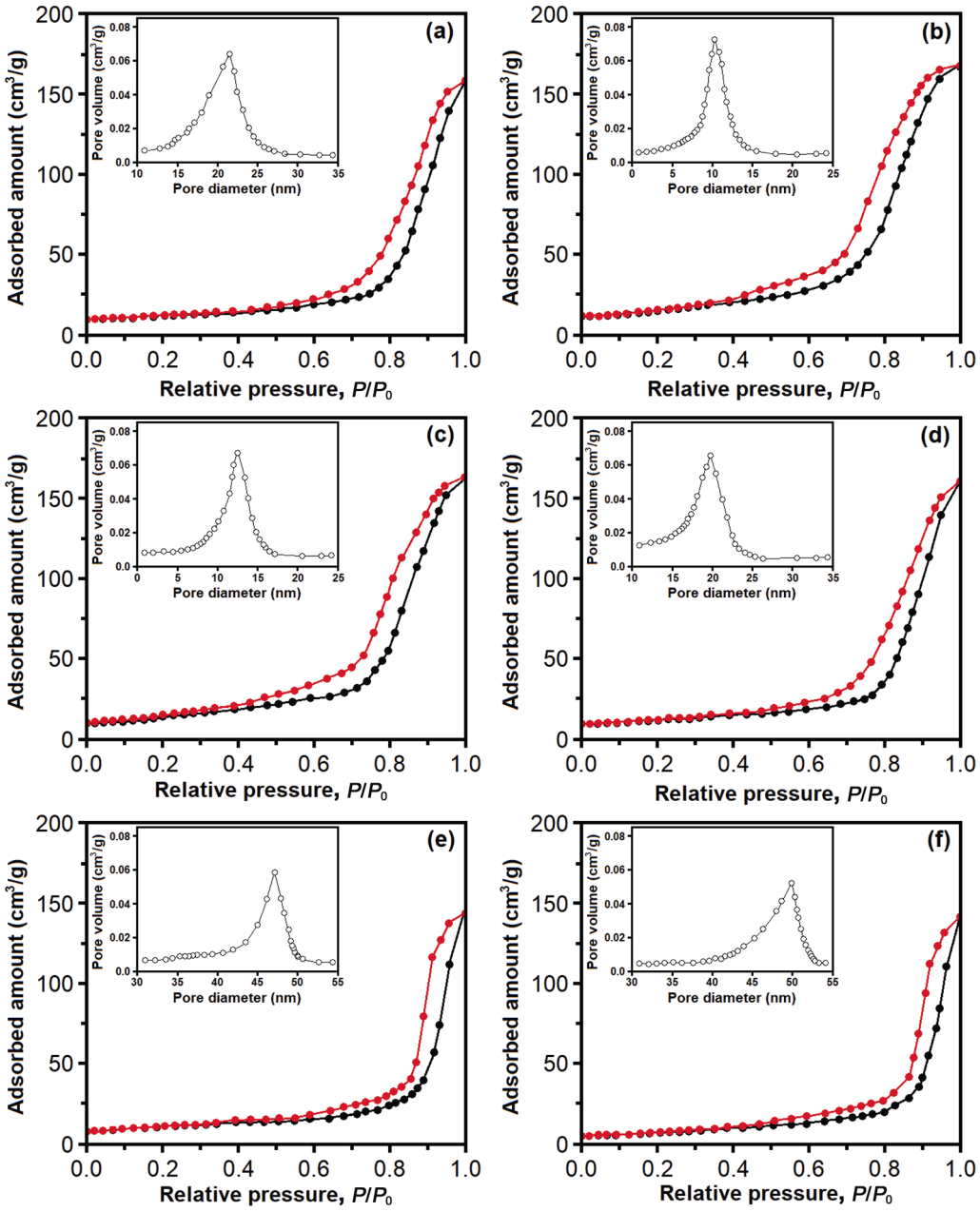

Fig. 5 N_2 adsorption/desorption isotherms and the corresponding Barrett–Joyner–Halenda (BJH) pore size distribution plots (insets) for (a) the undoped TiO_2 nanorod, and N–Fe codoped TiO_2 nanorods annealed at (b) 400 ℃, (c) 500 ℃, (d) 600 ℃, (e) 700 ℃, and (f) 800 ℃.

without any light illumination. However, under dark conditions no color removal was observed, indicating that absorbance changes over time is neglected.

In order to evaluate the effect of N–Fe codoped TiO_2 nanorods on the photocatalytic degradation of RhB under UV and visible-light irradiations, a blank experiment without catalyst material and in the presence N–Fe codoped TiO_2 nanorods annealed at 400, 500, 600, 700, and 800 ℃ compared with P25 and undoped TiO_2 nanorods was surveyed and the results are shown in Fig. 6. The experiments conducted without TiO_2 catalyst demonstrated that the degradation of RhB dye solution was extremely slow under UV light irradiation and no change in concentration under visible-light was observed. Therefore, the presence of both photocatalyst material and illumination are necessary for the efficient degradation. As can be seen from Figs. 6(a) and 6(b), the N–Fe codoped TiO_2 nanorods showed significant improvement in photocatalytic degradation of RhB when compared with P25 TiO_2 that is widely used as

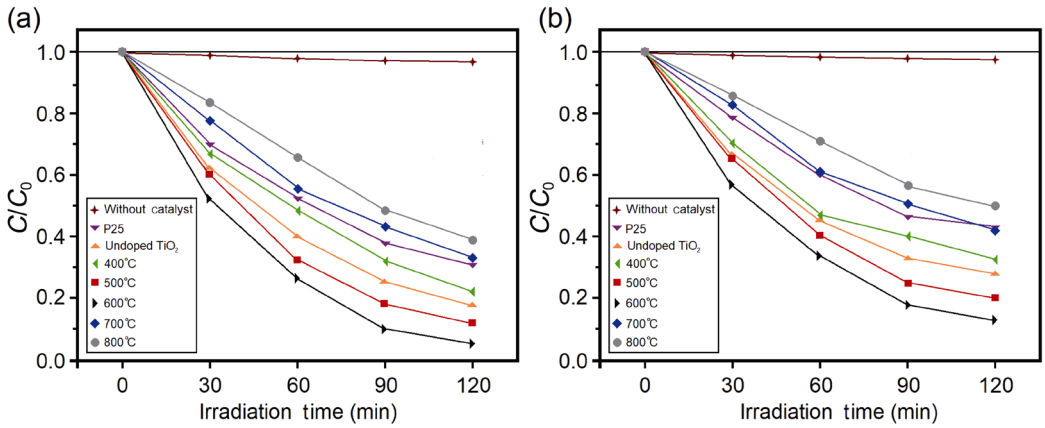

Fig. 6 Photocatalytic degradation of RhB solution without catalyst material and in presence of reference P25, undoped TiO_2 nanorod, and N–Fe codoped TiO_2 nanorods annealed at different temperatures under (a) UV light irradiation and (b) visible-light irradiation.

most efficient photocatalyst because of its phase composition [52]. The results exhibited that the concentration of RhB hardly changed under the visible-light irradiation over P25 due to the wavelength employed is insufficient to activate the pristine P25 TiO_2 nanoparticles. However, one dimensional morphology and large surface area of nanorods could provide the more active sites on the exposed surface and photocatalytic centers for the reactant molecules, higher absorption to organic pollutants, and lower recombination of electron–hole pairs which leads to a higher photocatalytic efficiency [53,54]. The N–Fe codoped TiO_2 nanorods annealed at 400 ℃ showed obvious photocatalytic activity because of the formation of anatase phase with enhanced crystallinity and the surface structure as explained before. With increasing annealing temperature from 400 to 600 ℃, although the relative crystallinity enhances and surface defect density decreases, the increase in crystallite size and decrease in specific surface area diminish the photoactivity of TiO_2 nanorods. It is well known that photo-induced decomposition of dye solution relied on the synergetic effects of several competitive or conflicting factors such as structural and textural characteristics, and surface properties [55]. A higher degree of crystallinity with fewer surface defects is beneficial for higher photocatalytic degradation performance in terms of facilitated charge carrier transform and hindered electron–hole recombination. It can be found that the N–Fe codoped TiO_2 nanorods annealed at 600 ℃, which contained a mixture of 79% anatase and 21% rutile, revealed the highest photocatalytic performance toward the degradation of RhB under both UV and visible-light among all tested TiO_2 samples, which could be good perspective for improving the photocatalytic degradation of RhB dye. These values after 120 min irradiation under UV and visible-light were 94.8% and 87.2%, respectively, which was observed to be above 1.37 and 1.52 times more efficient than P25 (69.1% and 57.4%) and above 1.15 and 1.2 times more efficient than undoped TiO_2 nanorods (82% and 72%). These results are in agreement with the work presented by Mahmoud *et al.* [56], in which they reported that a mixture of anatase and rutile of TiO_2 nanoparticles performs better photoactivity efficiency of MB as compared to pure anatase or rutile TiO_2.

Compared with undoped TiO_2 nanorods, the superior photocatalytic performance of N–Fe codoped TiO_2 nanorods may be ascribed to the N–Fe doped ions into TiO_2 nanorods, which favors the separation of photo-generated electron–hole pairs. It is well known that a small content of N or Fe ions can act as the trap sites for electrons and holes and inhibit the electron–hole recombination, which drastically improved the photocatalytic performance [35]. Li *et al.* [57] investigated the photocatalytic activity of methyl orange (MO) under visible light for N–Fe codoped TiO_2 nanoparticles synthesized by hydrothermal method. They found that the codoped TiO_2 owned higher photocatalytic efficiency (~96.4% degradation in 60 min) than pure TiO_2, N–TiO_2, Fe–TiO_2, and P-25, which was attributed to smaller particle size, larger specific surface area, and narrowed band gap. With increasing annealing temperature above 700 ℃, the photocatalytic activity of the N–Fe codoped TiO_2 nanorods steadily decreased. As a comparison, the changing trend of photocatalytic activities for the

nanorods tested under UV light and visible-light irradiations was similar to each other during increasing annealing temperature. N–Fe codoped TiO_2 nanorods annealed at 700 and 800 ℃ revealed 67% and 61.1% degradation of RhB under UV irradiation for 120 min, and 58.1% and 50% under visible-light irradiation, respectively. The annealing at 800 ℃ resulting in pure rutile nanorods with the lowest photocatalytic activity. The decrease in the photocatalytic efficiency of the samples annealed above 700 ℃ can be due to the following reasons. The phase transformation of anatase to rutile occurred and the nanorods are mainly composed of rutile. Also, increase in annealing temperature leads to growth of TiO_2 crystallites which results in the significant decrease of specific surface area of the nanorods, according to XRD and BET results. The large rutile crystals can also limit capability for the transfer of electron and hole between anatase and rutile, which results in the decrease in photodegradation [58].

On the other hand, the anatase phase of TiO_2 is generally considered the most active phase of photochemistry and has a high adsorption capacity of organic compounds on the surface than the rutile phase. The higher degradation rate of anatase could be explained by lower recombination rate of photogenerated electron–hole pairs. In contrast, thermodynamically stable rutile phase has a smaller energy bandgap (E_g), which allows excitation by wavelengths extending to visible range [59,60]. However, bandgap is one of the essential factors for photocatalytic activity, in which higher E_g provides better photodegradation property by more excitation of electron–hole pairs. In order to determine optical bandgap energy of N–Fe codoped TiO_2 nanorods, UV–vis absorption spectra were carried out as were displayed in Fig. 7. The results exhibited that the absorption edges are shifted to longer wavelengths as the annealing temperature elevated. The red shift of absorption edge wavelength can be attributed to the growth of crystallite size and the improvement of crystallinity. The bandgap energy (E_g) of samples was estimated from UV–vis spectra by plotting $(\alpha hv)^{0.5}$ as a function of the photon energy (hv), where α is the optical absorption coefficient, h is the Planck constant, and v is the frequency of the incident radiation [61,62]. The values of the E_g were accordingly determined by the linear extrapolation the high slope of the absorption curves (insets in Fig. 7). It can be observed that the bandgap energy of N–Fe codoped TiO_2 nanorods gradually reduced from 2.88 to 2.60 eV, when the annealing temperature increased from 400 to 800 ℃, compared to 3.12 eV for undoped TiO_2 nanorod and 3.15 eV for the reference P25 [63]. It seems that codoping narrows the TiO_2 bandgap and is the main cause of the large red shift [64]. On the other hand, the phase transformation and increase in crystallite size is the dominate progress, which leads to reduce in the E_g with increasing the annealing temperature [65]. According to Wang *et al.* [66], the band gap of P25 samples monotonically decreased with increasing calcination temperature due to the following factors: (1) increase in the crystallite size; (2) phase transformation from anatase to rutile. These authors reported a proportional increase in photocatalytic activity of MO under UV light irradiation with increased calcination temperature up to 500 ℃. Degradation rate of the most organic compounds is described by pseudo first-order kinetics [67]:

$$-\frac{dC}{dt} = kC \tag{3}$$

In this equation, k is the reaction rate constant (min^{-1}) and is affected by dye stuff concentration. By integration of Eq. (3) with the boundary conditions of $C = C_0$ at $t = 0$, it leads to Eq. (4):

$$-\ln\frac{C}{C_0} = kt \tag{4}$$

where C_0 is the initial concentration before irradiation, C is the dye concentration at each irradiated time interval, and t is the time irradiation (min).

The pseudo first-order kinetics plots of $\ln(C/C_0)$ versus irradiation time for RhB dye aqueous solution, which describes photocatalytic reactions for the different studied catalysts under UV and visible-light are displayed in Fig. 8. Due to the exponential reduction of RhB concentration in this model, a linear relationship between the logarithmic curves of relative concentration and reaction time is defined as ordinate and abscissa. Hence, in this case, the best line always fitted which meets the data. The values of k as a characteristic of photocatalyst activity can be obtained directly by the slope of plots of $\ln(C_t/C_0)$ versus t which are summarized in Table 2. The calculated results manifest that the apparent rate constants are equal to 0.0098, 0.0142, 0.0125, 0.0180, 0.0256, 0.0093, and 0.0081 min^{-1} under UV light irradiation for the P25, undoped TiO_2 nanorods and N–Fe codoped TiO_2 nanorods annealed at 400, 500, 600, 700, and 800 ℃, respectively. These values were estimated to be 0.0075, 0.0108, 0.0094,

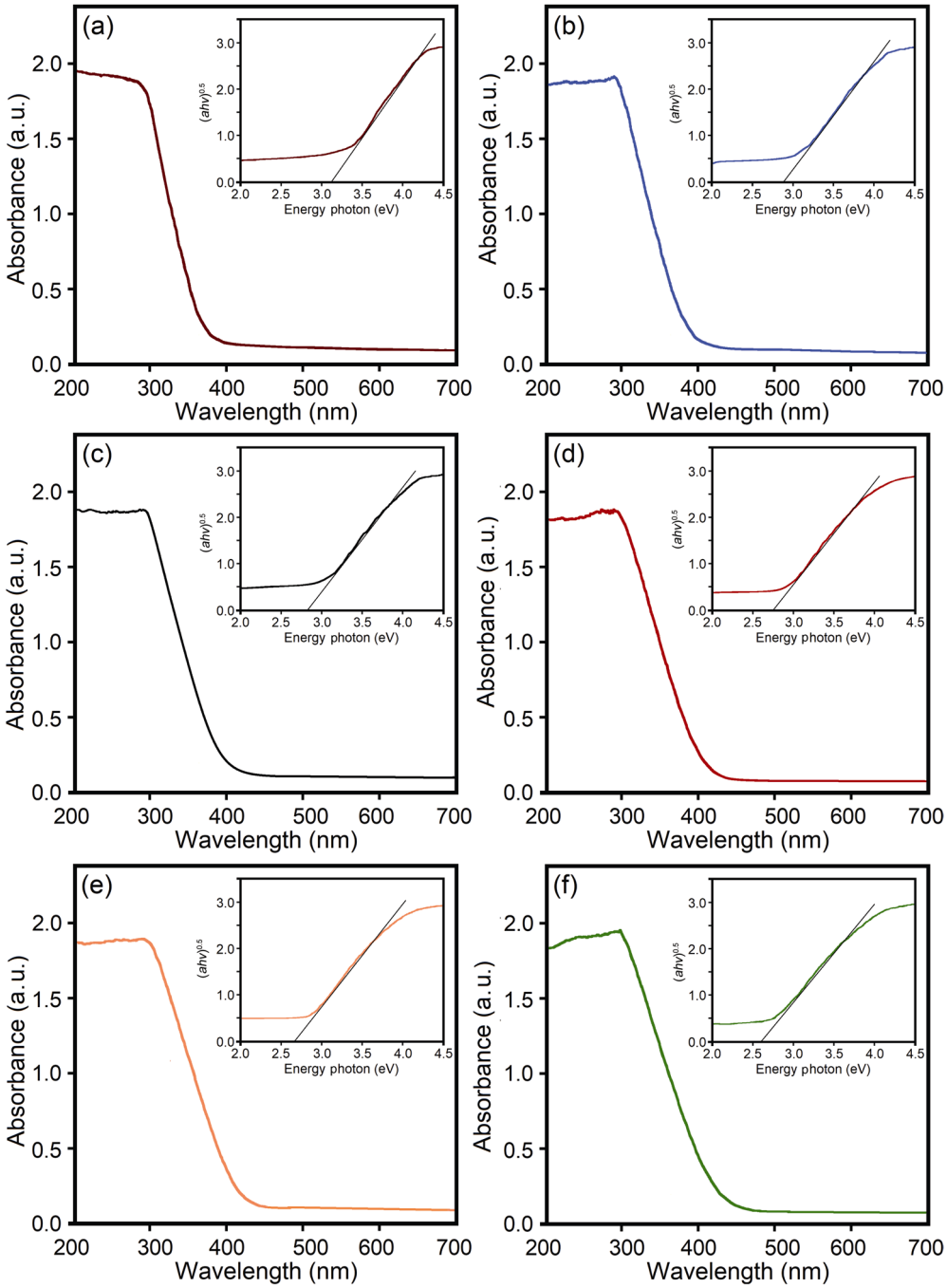

Fig. 7 UV–vis absorbance spectra of (a) the undoped TiO_2 nanorod and N–Fe codoped TiO_2 nanorods annealed at (b) 400 ℃, (c) 500 ℃, (d) 600 ℃, (e) 700 ℃, and (f) 800 ℃. The insets present corresponding plots of $(\alpha hv)^{0.5}$ versus photon energy (hv) for nanorods.

0.0139, 0.0176, 0.0074, and 0.0060 min^{-1} under visible-light irradiation. The degradation rate of RhB dye solution increased linearly with increasing irradiation time. Meanwhile, the annealing has a significant effect on the degradation rates, as for the N–Fe codoped TiO_2 nanorods annealed at 600 ℃ displayed the highest degradation rate constant for both UV and visible-light irradiations, which is about 2.7 and 2.35 times compared with P25, under the same conditions. Based on the obtained results, it can be concluded that the photocatalytic degradation efficiency of RhB under both UV and visible-light follows the order samples annealed at 600 ℃ > 500 ℃ > 400 ℃ > undoped TiO_2 > P25 > 700 ℃ > 800 ℃ > without catalyst. Yang *et al.* [68] evaluated the photocatalytic activity of C-, S-, N-, and Fe-doped TiO_2 by photocatalytic

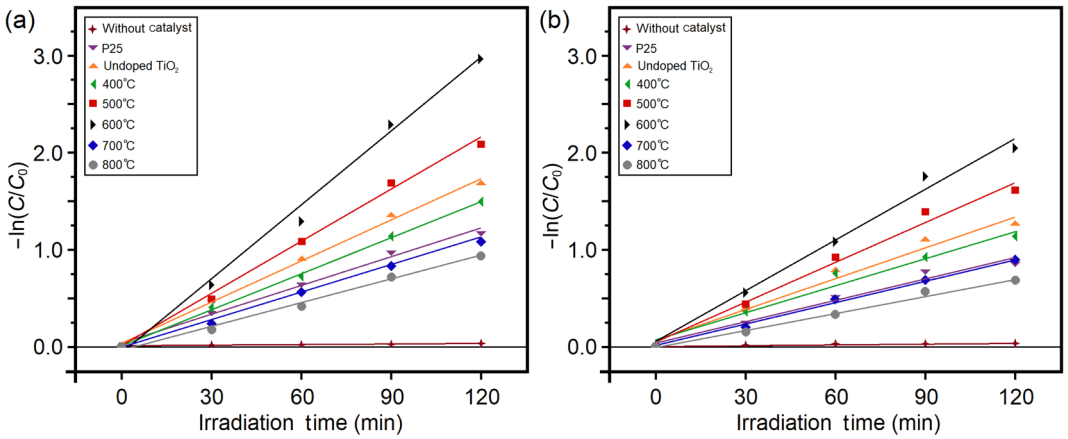

Fig. 8 First-order kinetics plots for the photocatalytic degradation of RhB without catalyst material and in presence of reference P25, undoped TiO_2 nanorod, and N–Fe codoped TiO_2 nanorods annealed at different temperatures under (a) UV light irradiation and (b) visible-light irradiation.

Table 2 Values of apparent rate constant k and R^2 for the different samples

Sample	k (min^{-1})		R^2	
	UV irradiation	Visible irradiation	UV irradiation	Visible irradiation
TiO_2-P25	0.0098	0.0075	0.997	0.992
Undoped TiO_2-600 ℃	0.0142	0.0108	0.995	0.979
N–Fe–TiO_2-400 ℃	0.0125	0.0094	0.992	0.972
N–Fe–TiO_2-500 ℃	0.0180	0.0139	0.996	0.987
N–Fe–TiO_2-600 ℃	0.0256	0.0176	0.994	0.990
N–Fe–TiO_2-700 ℃	0.0093	0.0074	0.997	0.976
N–Fe–TiO_2-800 ℃	0.0081	0.0060	0.993	0.992

degradation of RhB under visible-light irradiation. According to the kinetic model, they obtained the rate constants of 0.0010, 0.0016, 0.0029, and 0.0019 min^{-1} for CNS–xFe–TiO_2 with x equals 0, 0.1, 0.3, and 0.5, respectively.

Since the purpose behind was photocatalytic behavior of RhB dye solution, not only the degradation rate of RhB was determined, but also the photogeneration properties of CO_2 were investigated. Figures 9(a) and 9(b) illustrate the concentration of generated CO_2 without catalyst material and N–Fe codoped TiO_2 nanorods annealed at different temperatures compared to P25 and undoped TiO_2 nanorods under UV and visible-light irradiations. The concomitant increase in concentration of CO_2 could be seen with continuous decrease of RhB under irradiation. The lowest and highest generation rates of CO_2 were shown by the N–Fe codoped TiO_2 nanorods annealed at 800 and 600 ℃, respectively. In the case of P25, the generation rate of CO_2 was relatively low when compared to nanorods annealed at 400, 500, and 600 ℃. Additionally, the CO_2 concentration increased as the illumination time increased, indicating it to be an actual sensitized photocatalytic reaction. When the photocatalysis was carried out with visible-light irradiation, production of CO_2 was less than the UV light irradiation.

4 Conclusions

In conclusion, the aligned N–Fe codoped TiO_2 nanorods with an average diameter of 100 nm were successfully synthesized by a simple liquid-phase deposition process combined with a template-assisted approach. The synergetic effects of phase structure, BET surface area, and crystallinity induced by different annealing temperatures on the photocatalytic activities of nanorods for the degradation of RhB dye under UV and visible-light ($\lambda \geqslant 420$ nm) irradiations were investigated. Experimental results indicated that the N–Fe codoped TiO_2 nanorods annealed at 600 ℃ with mixed anatase (79%) and rutile phases (21%) have the highest photocatalytic performance among the series of nanorods. These nanorods showed photocatalytic degradation rate of RhB about 2.35 times higher under visible-light as compared to Degussa P25 TiO_2, which is a standard material in the field of photocatalytic reactions. The enhanced photocatalytic degradation of nanorods can be mainly related to higher exposed surface areas and one dimensional (1D) structure-related properties, which leads to more reactive species in contact with the dye, improved electron transport, and effective separation of photogenerated carriers. With

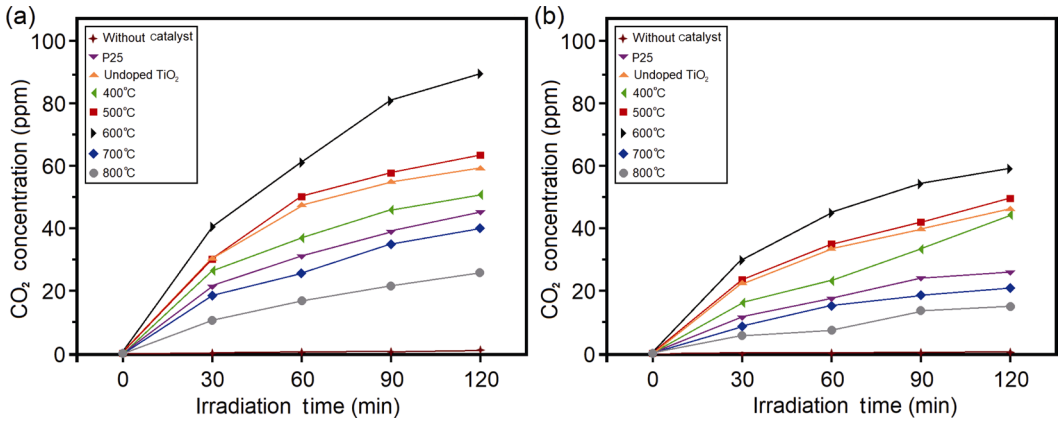

Fig. 9 Photogeneration of CO_2 from RhB solution without catalyst material, and by using reference P25, undoped TiO_2 nanorod, and N–Fe codoped TiO_2 nanorods annealed at different temperatures under (a) UV light irradiation and (b) visible-light irradiation.

increasing annealing temperature over 700 ℃, the photocatalytic activity of nanorods decreased, which is caused by more formation of rutile phase, decrease of surface area, and growth of crystallites. However, it was found that the photocatalytic degradation efficiency of RhB under both UV and visible-light follows the order samples annealed at 600 ℃ > 500 ℃ > undoped TiO_2 > 400 ℃ > P25 > 700 ℃ > 800 ℃ > without catalyst.

References

[1] Luo CZ, Ren XH, Dai ZG, *et al*. Present perspectives of advanced characterization techniques in TiO_2-based photocatalysts. *ACS Appl Mater Interfaces* 2017, **9**: 23265–23286.

[2] Ahmed SN, Haider W. Heterogeneous photocatalysis and its potential applications in water and wastewater treatment: A review. *Nanotechnology* 2018, **29**: 342001.

[3] Tang B, Chen HQ, Peng HP, *et al*. Graphene modified TiO_2 composite photocatalysts: Mechanism, progress and perspective. *Nanomaterials* 2018, **8**: 105–132.

[4] Liang YT, Vijayan BK, Lyandres O, *et al*. Effect of dimensionality on the photocatalytic behavior of carbon–titania nanosheet composites: Charge transfer at nanomaterial interfaces. *J Phys Chem Lett* 2012, **3**: 1760–1765.

[5] Sulaiman SNA, Zaky Noh M, Nadia Adnan N, *et al*. Effects of photocatalytic activity of metal and non-metal doped TiO_2 for hydrogen production enhancement—A review. *J Phys: Conf Ser* 2018, **1027**: 012006.

[6] Mohini R, Lakshminarasimhan N. Coupled semiconductor nanocomposite g-C_3N_4/TiO_2 with enhanced visible light photocatalytic activity. *Mater Res Bull* 2016, **76**: 370–375.

[7] Mondal K, Ali MA, Agrawal VV, *et al*. Highly sensitive biofunctionalized mesoporous electrospun TiO_2 nanofiber based interface for biosensing. *ACS Appl Mater Interfaces* 2014, **6**: 2516–2527.

[8] Sadeghzadeh-Attar A, Bafandeh MR. Effect of annealing on UV–visible absorption and photoluminescence behavior of liquid phase deposited TiO_2 nanorods. *Int J Appl Ceram Technol* 2019, **16**: 2429–2440.

[9] Sadeghzadeh-Attar A. Structural and optical characteristic of single crystal rutile-titania nanowire arrays prepared in alumina membranes. *Mater Chem Phys* 2016, **182**: 148–154.

[10] Wen W, Wu JM, Jiang YZ, *et al*. Anatase TiO_2 ultrathin nanobelts derived from room-temperature-synthesized titanates for fast and safe lithium storage. *Sci Rep* 2015, **5**: 11804.

[11] Liu ZY, Misra M. Dye-sensitized photovoltaic wires using highly ordered TiO_2 nanotube arrays. *ACS Nano* 2010, **4**: 2196–2200.

[12] Ge MZ, Cao CY, Huang JY, *et al*. A review of one-dimensional TiO_2 nanostructured materials for environmental and energy applications. *J Mater Chem A* 2016, **4**: 6772–6801.

[13] Xu Y, Wen W, Wu JM. Titania nanowires functionalized polyester fabrics with enhanced photocatalytic and antibacterial performances. *J Hazard Mater* 2018, **343**: 285–297.

[14] Richter C, Schmuttenmaer CA. Exciton-like trap states limit electron mobility in TiO_2 nanotubes. *Nat Nanotech* 2010, **5**: 769–772.

[15] Luan XN, Guan DS, Wang Y. Facile synthesis and morphology control of bamboo-type TiO_2 nanotube arrays for high-efficiency dye-sensitized solar cells. *J Phys Chem C* 2012, **116**: 14257–14263.

[16] Wehrenfennig C, Palumbiny CM, Snaith HJ, *et al*. Fast charge-carrier trapping in TiO_2 nanotubes. *J Phys Chem C* 2015, **119**: 9159–9168.

[17] Wang XX, He GF, Fong H, *et al*. Electron transport and recombination in photoanode of electrospun TiO_2 nanotubes for dye-sensitized solar cells. *J Phys Chem C*

2013, **117**: 1641–1646.

[18] Liu K, Lin SW, Liao JJ, *et al*. Synthesis and characterization of hierarchical structured TiO_2 nanotubes and their photocatalytic performance on methyl orange. *J Nanomater* 2015, **2015**, Article ID 201650.

[19] Shoja A, Nourmohammadi A, Feiz MH. Growth of TiO_2 nanotube arrays in semiconductor porous anodic alumina templates. *J Mater Res* 2014, **29**: 2432–2440.

[20] Sadeghzadeh Attar A, Sasani Ghamsari M, Hajiesmaeilbaigi F, *et al*. Study on the effects of complex ligands in the synthesis of TiO_2 nanorod arrays using the sol–gel template method. *J Phys D: Appl Phys* 2008, **41**: 155318.

[21] Karaman M, Sarıipek F, Köysüren Ö, *et al*. Template assisted synthesis of photocatalytic titanium dioxide nanotubes by hot filament chemical vapor deposition method. *Appl Surf Sci* 2013, **283**: 993–998.

[22] Liang YC, Wang CC, Kei CC, *et al*. Photocatalysis of Ag-loaded TiO_2 nanotube arrays formed by atomic layer deposition. *J Phys Chem C* 2011, **115**: 9498–9502.

[23] Lee JH, Leu IC, Hsu MC, *et al*. Fabrication of aligned TiO_2 one-dimensional nanostructured arrays using a one-step templating solution approach. *J Phys Chem B* 2005, **109**: 13056–13059.

[24] Sadeghzadeh-Attar A, Akhavan-Safaei I, Bafandeh MR. UV–visible absorption and photoluminescence characteristics of SnO_2 nano-tube/wire arrays fabricated by LPD method. *Int J Appl Ceram Technol* 2018, **15**: 1084–1094.

[25] Resasco J, Zhang H, Kornienko N, *et al*. TiO_2/$BiVO_4$ nanowire heterostructure photoanodes based on type II band alignment. *ACS Cent Sci* 2016, **2**: 80–88.

[26] Nischk M, Mazierski P, Wei ZS, *et al*. Enhanced photocatalytic, electrochemical and photoelectrochemical properties of TiO_2 nanotubes arrays modified with Cu, AgCu and Bi nanoparticles obtained via radiolytic reduction. *Appl Surf Sci* 2016, **387**: 89–102.

[27] Pham VV, Bui DP, Tran HH, *et al*. Photoreduction route for Cu_2O/TiO_2 nanotubes junction for enhanced photocatalytic activity. *RSC Adv* 2018, **8**: 12420–12427.

[28] Viet PV, Phan BT, Mott D, *et al*. Silver nanoparticle loaded TiO_2 nanotubes with high photocatalytic and antibacterial activity synthesized by photoreduction method. *J Photochem Photobiol A: Chem* 2018, **352**: 106–112.

[29] González-Torres JC, Poulain E, Domínguez-Soria V, *et al*. C-, N-, S-, and F-doped anatase TiO_2 (101) with oxygen vacancies: Photocatalysts active in the visible region. *Int J Photoenergy* 2018, **2018**, Article ID 7506151.

[30] Gul SR, Khan M, Wu B, *et al*. Combined experimental and theoretical study of visible light active P doped TiO_2 photocatalyst. *Mater Res Express* 2017, **4**: 065502.

[31] Sadeghzadeh-Attar A. Preparation and enhanced photocatalytic activity of Co/F codoped tin oxide nanotubes/nanowires: A wall thickness-dependence study. *Appl Phys A* 2019, **125**: 768.

[32] Wang SN, Yuan RF, Zhou BH, *et al.* Effects of metal ion-doping on the characteristics and photocatalytic activities of TiO_2 nanotubes. *Funct Mater* 2018, **25**: 282–288.

[33] Solís-Casados DA, Escobar-Alarcón L, Alvarado-Pérez V, *et al*. Photocatalytic activity under simulated sunlight of Bi-modified TiO_2 thin films obtained by sol gel. *Int J Photoenergy* 2018, **2018**, Article ID 8715987.

[34] Yang Y, Kao LC, Liu YY, *et al*. Cobalt-doped black TiO_2 nanotube array as a stable anode for oxygen evolution and electrochemical wastewater treatment. *ACS Catal* 2018, **8**: 4278–4287.

[35] Cheng HH, Chen SS, Yang SY, *et al*. Sol-gel hydrothermal synthesis and visible light photocatalytic degradation performance of Fe/N codoped TiO_2 catalysts. *Materials* 2018, **11**: 939.

[36] Peng FC, Gao HL, Zhang GL, *et al*. Synergistic effects of Sm and C co-doped mixed phase crystalline TiO_2 for visible light photocatalytic activity. *Materials* 2017, **10**: 209.

[37] Zhang M, Wu J, Lu DD, *et al*. Enhanced visible light photocatalytic activity for TiO_2 nanotube array films by codoping with tungsten and nitrogen. *Int J Photoenergy* 2013, **2013**, Article ID 471674.

[38] Samet L, March K, Stephan O, *et al*. Radiocatalytic Cu-incorporated TiO_2 nano-particles for the degradation of organic species under gamma irradiation. *J Alloys Compd* 2018, **743**: 175–186.

[39] Sadeghzadeh Attar A, Hassani Z. Fabrication and growth mechanism of single-crystalline rutile TiO_2 nanowires by liquid-phase deposition process in a porous alumina template. *J Mater Sci Technol* 2015, **31**: 828–833.

[40] Yu JG, Yu HG, Cheng B, *et al*. The effect of calcination temperature on the surface microstructure and photocatalytic activity of TiO_2 thin films prepared by liquid phase deposition. *J Phys Chem B* 2003, **107**: 13871–13879.

[41] Zhang HZ, Banfield JF. Understanding polymorphic phase transformation behavior during growth of nanocrystalline aggregates: Insights from TiO_2. *J Phys Chem B* 2000, **104**: 3481–3487.

[42] Dam T, Jena SS, Pradhan DK. Equilibrium state of anatase to rutile transformation for nano-structured titanium dioxide powder using polymer template method. *IOP Conf Ser: Mater Sci Eng* 2016, **115**: 012038.

[43] Boehme M, Ensinger W. Mixed phase anatase/rutile titanium dioxide nanotubes for enhanced photocatalytic degradation of methylene-blue. *Nano-Micro Lett* 2011, **3**: 236–241.

[44] Li D, Haneda H, Hishita S, *et al*. Visible-light-driven N–F-codoped TiO_2 photocatalysts. 1. Synthesis by spray pyrolysis and surface characterization. *Chem Mater* 2005, **17**: 2588–2595.

[45] Tian F, Wu ZS, Tong YB, *et al*. Microwave-assisted synthesis of carbon-based (N, Fe)-codoped TiO_2 for the photocatalytic degradation of formaldehyde. *Nanoscale Res Lett* 2015, **10**: 360.

[46] Khan H, Swati IK. Fe^{3+}-doped anatase TiO_2 with d–d transition, oxygen vacancies and Ti^{3+} centers: Synthesis, characterization, UV–vis photocatalytic and mechanistic studies. *Ind Eng Chem Res* 2016, **55**: 6619–6633.

[47] Jiang YB, Mi WB, Jiang EY, *et al*. Structure, optical, and magnetic properties of facing-target reactive sputtered $Ti_{1-x}Fe_xO_{2-\delta}$ films. *J Vac Sci Technol A: Vac Surfaces Films* 2009, **27**: 1172–1177.

[48] Tayeb AM, Hussein DS. Synthesis of TiO_2 nanoparticles and their photocatalytic activity for methylene blue. *American Journal of Nanomaterials* 2015, **3**: 57–63.

[49] Ai HY, Shi JW, Duan RX, *et al*. Sol-gel to prepare nitrogen doped TiO_2 nanocrystals with exposed {001} facets and high visible-light photocatalytic performance. *Int J Photoenergy* 2014, **2014**, Article ID 724910.

[50] Thommes M, Kaneko K, Neimark AV, *et al*. Physisorption of gases, with special reference to the evaluation of surface area and pore size distribution (IUPAC Technical Report). *Pure Appl Chem* 2015, **87**: 1051–1069.

[51] Zhang JR, Gao L. Synthesis and characterization of nanocrystalline tin oxide by sol–gel method. *J Solid State Chem* 2004, **177**: 1425–1430.

[52] Pierpaoli M, Favoni O, Fava G, *et al*. A novel method for the combined photocatalytic activity determination and bandgap estimation. *Methods Protoc* 2018, **1**: 22.

[53] Jiang F, Zheng SR, Zheng Z, *et al*. Photo-degradation of Acid-red 3B dye catalyzed by TiO_2 nanotubes. *J Environ Sci* 2006, **18**: 783–787.

[54] Sadeghzadeh-Attar A. Efficient photocatalytic degradation of methylene blue dye by SnO_2 nanotubes synthesized at different calcination temperatures. *Sol Energy Mater Sol Cells* 2018, **183**: 16–24.

[55] Yang CX, Zhang M, Dong WP, *et al*. Highly efficient photocatalytic degradation of methylene blue by PoPD/TiO_2 nanocomposite. *PLoS One* 2017, **12**: e0174104.

[56] Mahmoud HA, Narasimharao K, Ali TT, *et al*. Acidic peptizing agent effect on anatase-rutile ratio and photocatalytic performance of TiO_2 nanoparticles. *Nanoscale Res Lett* 2018, **13**: 48–61.

[57] Li X, Chen ZM, Shi YC, *et al*. Preparation of N, Fe co-doped TiO_2 with visible light response. *Powder Technol* 2011, **207**: 165–169.

[58] Hyett G, Green M, Parkin IP. X-ray diffraction area mapping of preferred orientation and phase change in TiO_2 thin films deposited by chemical vapor deposition. *J Am Chem Soc* 2006, **128**: 12147–12155.

[59] Fischer K, Gawel A, Rosen D, *et al*. Low-temperature synthesis of anatase/rutile/brookite TiO_2 nanoparticles on a polymer membrane for photocatalysis. *Catalysts* 2017, **7**: 209–222.

[60] Hurum DC, Agrios AG, Gray KA, *et al*. Explaining the enhanced photocatalytic activity of degussa P25 mixed-phase TiO_2 using EPR. *J Phys Chem B* 2003, **107**: 4545–4549.

[61] Hajijafari Bidgoli S, Sadeghzadeh Attar A, Bafandeh MR. Structural and optical properties of Sr-modified bismuth silicate nanostructured films synthesized by sol gel method. *J Nanostruct* 2017, **7**: 258–265.

[62] Sadeghzadeh-Attar A, Bafandeh MR. The effect of annealing temperature on the structure and optical properties of well-aligned 1D SnO_2 nanowires synthesized using template-assisted deposition. *CrystEngComm* 2018, **20**: 460–469.

[63] Scarsella M, Bracciale MP, de Caprariis B, *et al.* Improved photocatalytic properties of doped titanium-based nanometric oxides. *Chem Eng Trans* 2017, **60**: 133–138.

[64] Lai LL, Wu JM. A facile solution approach to W, N co-doped TiO_2 nanobelt thin films with high photocatalytic activity. *J Mater Chem A* 2015, **3**: 15863–15868.

[65] Khalifa ZS. Grain size reduction on nanostructured TiO_2 thin films due to annealing. *RSC Adv* 2017, **7**: 30295–30302.

[66] Wang GH, Xu L, Zhang J, *et al*. Enhanced photocatalytic activity of powders (P25) via calcination treatment. *Int J Photoenergy* 2012, **2012**, Article ID 265760.

[67] Zhang J, Cai YB, Hou XB, *et al*. Preparation of TiO_2 nanofibrous membranes with hierarchical porosity for efficient photocatalytic degradation. *J Phys Chem C* 2018, **122**: 8946–8953.

[68] Yang XX, Cao CD, Erickson L, *et al*. Photo-catalytic degradation of Rhodamine B on C-, S-, N-, and Fe-doped TiO_2 under visible-light irradiation. *Appl Catal B: Environ* 2009, **91**: 657–662.

Open Access This article is licensed under a Creative Commons Attribution 4.0 International License, which permits use, sharing, adaptation, distribution and reproduction in any medium or format, as long as you give appropriate credit to the original author(s) and the source, provide a link to the Creative Commons licence, and indicate if changes were made.

The images or other third party material in this article are included in the article's Creative Commons licence, unless indicated otherwise in a credit line to the material. If material is not included in the article's Creative Commons licence and your intended use is not permitted by statutory regulation or exceeds the permitted use, you will need to obtain permission directly from the copyright holder.

To view a copy of this licence, visit http://creativecommons.org/licenses/by/4.0/.